Near-Infrared Spectroscopy of Molecular Filaments in the Reflection Nebula NGC 7023

Paul Martini, K. Sellgren

Department of Astronomy, 174 W. 18th Ave., Ohio State University,
Columbus, OH 43210
martini,sellgren@payne.mps.ohio-state.edu

and

Joseph L. Hora

Institute for Astronomy, University of Hawaii, Honolulu, HI 96822
hora@galileo.ifa.hawaii.edu

Abstract

We present near-infrared spectroscopy of fluorescent molecular hydrogen (H_2) emission from molecular filaments in the reflection nebula NGC 7023. We derive the relative column densities of H_2 rotational-vibrational states from the measured line emission and compare these results with several model photodissociation regions covering a range of densities, incident UV-fields, and excitation mechanisms. Our best-fit models for one filament suggest, but do not require, either a combination of different densities, suggesting clumps of 10^6 cm^{-3} in a $10^4 - 10^5$ cm^{-3} filament, or a combination of fluorescent excitation and thermally-excited gas, perhaps due to a shock from a bipolar outflow. We derive densities and UV fields for these molecular filaments that are in agreement with previous determinations.

Subject headings: infrared: spectra — interstellar: molecules — infrared: sources — nebulae: reflection — nebulae: individual (NGC 7023)

1. Introduction

Near-infrared spectroscopic measurements of the relative line strengths of molecular hydrogen (H_2) are a powerful way to determine the densities, incident ultraviolet (UV) radiation field, and excitation mechanisms present in photodissociation regions (PDRs). H_2 emission, attributed to shocks, was first detected in the planetary nebula NGC 7027 and the Orion Nebula (Treffers et al. 1976; Gautier et al. 1976). UV-pumped fluorescent molecular hydrogen was first detected in the reflection nebula NGC 2023 (Gatley et al. 1987; Sellgren 1986).

Measurements of the relative and absolute intensities of rotational-vibrational transitions in H_2 can be readily analyzed with respect to existing models for collisional and fluorescent excitation. These static models include UV-illuminated, low-density clouds (Black & van Dishoeck 1987), UV-illuminated, high-density clouds (Sternberg & Dalgarno 1989; Draine & Bertoldi 1996), UV-illuminated, clumpy clouds (Burton, Hollenbach, & Tielens 1990), and shocked clouds (Hollenbach & McKee 1979, 1989; Brand et al. 1988; Brand et al. 1989). Application of PDR models to NGC 2023 confirmed that UV-pumped fluorescence is likely the dominant excitation mechanism (Black & van Dishoeck 1987; Burton et al. 1990; Draine & Bertoldi 1996). These PDR models are applicable to a wide variety of objects such as HII regions (e.g. Orion), planetary nebulae (e.g. NGC 7027) as well as other reflection nebulae (Black & van Dishoeck 1987; Sternberg & Dalgarno 1989). Recent work by Goldschmidt & Sternberg (1995) has shown that time-dependent PDR models may be required as well, a scenario these authors apply to NGC 2023.

We present near-infrared spectroscopy of H_2 emission in NGC 7023, a reflection nebula which is similar in many ways to NGC 2023. One difference, however, is that NGC 2023 is illuminated by a main-sequence B star, while NGC 7023 is illuminated by a pre-main-sequence B star, the Herbig Ae/Be star HD 200775.

Chokshi et al. (1988) observed emission in atomic fine-structure lines of NGC 7023, which represents the bulk of the cooling mechanism of most PDRs (Tielens & Hollenbach 1986; Hollenbach et al. 1991). Their grid of measurements of [O I] (63 μm) and [C II] (158 μm), with beam diameters of $33''$ and $55''$, respectively, were centered on a region $30''$ N, $20''$ W of the central star. Their PDR model yields a peak density of $\sim 4 \times 10^3 \mathrm{cm}^{-3}$ surrounded by a lower density, ~ 500 cm^{-3} region where CO (Watt et al. 1986) is formed. Based upon their line measurements, they also derive an incident UV field of $G_0 = 2.6 \times 10^3$ in the units of Habing (1968) where Habing estimated the interstellar UV flux to be 1.2×10^{-4} ergs cm^{-2} s^{-1} sr^{-1}.

Rogers et al. (1995) compare H I, CO, and IRAS observations of NGC 7023 taken

with a resolution of approximately $1'$. The peak in atomic hydrogen emission agrees with the peak in the fine-structure lines observed by Chokshi et al. (1988). However, Rogers et al. (1995) also find a molecular rim surrounding the atomic region and a high contrast in densities between the atomic and molecular regions. They find similar ($\sim 10^4$ cm^{-3}) molecular densities to those reported by Chokshi et al. (1988) when using equilibrium PDR models. They also compared their observations to time-dependent models and they find no evidence for either a non-equilibrium PDR or an active bipolar outflow. Rather they propose that an outflow in the past paved the way for the development of the current low-density PDR.

The presence of a bipolar outflow in NGC 7023 has long been a matter of some debate. Watt et al. (1986) mapped the nebula in both the ^{12}CO and ^{13}CO $J = 1 - 0$ transitions with a half-power beamwidth of $1'$ and found morphological features characteristic of an outflow source, though they did not have sufficient signal-to-noise to resolve high-velocity wings in their spectra. They also report a molecular hydrogen density of $\sim 5 \times 10^4$ cm^{-3} in the shell surrounding the cavity in the molecular emission. Fuente et al. (1993) mapped NGC 7023 at higher angular resolution ($11''$ to $26''$ half-power beamwidth) in a number of molecular millimeter lines, including HCO$^+$, and found evidence for gas densities of up to $\sim 10^5$cm^{-3}. High resolution maps of NGC 7023 in HCO$^+$ and HI, in particular of the molecular rim surrounding the cavity containing atomic gas, by Fuente et al. (1996) have found four high-density molecular filaments with velocities from 1.9 to 4.0 km s^{-1}. These HCO$^+$ filaments match the filaments shown in optical polarization color images (Watkin, Gledhill, & Scarrott 1991), 2.1 μm broadband images (Sellgren, Werner, & Dinerstein 1992), narrowband images of $1 - 0$ S(1) H$_2$ emission (LeMaire et al. 1996), and mid-IR images (Cesarsky et al. 1996). Fuente et al. (1996) estimate the density of these filaments to be $\sim 10^5$ cm^{-3} from the fractional abundance of HCO$^+$. This is a factor of $10 - 25$ times greater than the densities reported by Chokshi et al. (1988) and Rogers et al. (1995) at lower spatial resolution.

2. Observations

The observations of NGC 7023 discussed in this paper were made on 1993 July 5 with (FWHM) source sizes of $\sim 1''.4 \times 0''.9$ (including seeing and all instrumental effects) at the University of Hawaii's 2.2-m telescope on Mauna Kea with KSPEC (Hodapp et al. 1994). This instrument provides medium resolution, cross-dispersed spectra from 1 to 2.5 μm with an $0''.6 \times 6''.5$ slit oriented NS. At K, our spectral resolution was 30 Å ($R = \lambda/\Delta\lambda = 730$)

and the dispersion was 20 Å pixel^{-1}, leading to undersampled spectra. At H, our spectral resolution was 23 Å ($R = 720$) and the dispersion was 15 Å pixel^{-1}. The instrument makes use of two 256×256 NICMOS3 arrays, one for spectroscopic information and the other to provide imaging of the region around the slit for tracking purposes.

Two different positions in the nebula were observed, both centered on relatively bright regions. The first is located $40''$ W, $34''$ N (hereafter Position 1) of the central star, HD 200775; the second is on a somewhat fainter filament $22''$ W, $66''$ S (hereafter Position 2) of the central star. Three 150s integrations were taken of each position and summed together. The offset induced in the slit position by sky chopping $300''$ N between integrations was found to be negligibly small compared to the width of the filaments ($\gtrsim 6''$). Spectra of three A0 stars, SAO 19255, HR 8300, and the photometric standard HD 203856 (Elias et al. 1982), were then taken for use in flux calibration and atmospheric correction. Using our spectra and narrowband images obtained by A. Quillen, we estimate the absolute uncertainty in our flux calibration to be a factor of 2.4 (1σ).

Figures 1 and 2 show the final reduced spectra. The data were reduced using the OSU implementation of VISTA (Stover 1988) by first straightening the spectra along the slit using the centroid of the object and then summing over a $5''$ wide portion of the $J, H,$ and K bands. The spectra were wavelength calibrated with an Argon lamp, resulting in a calibration to vacuum wavelengths (e.g. Black & van Dishoeck 1987).

The line strengths of the reduced and extracted (but not unreddened) spectra were measured using the OSU LINER package. We achieved a signal-to-noise approaching 20 for the strongest lines and 10 for the weaker lines (see Table 1) in the K Band, where this instrument is most sensitive. Our relative lin intensities are therefore better determined than the absolute intensities. Lower quality detections were made in H due to a combination of lower sensitivity, blending of the H_2 lines, and difficulty subtracting the night-sky OH airglow emission lines. We report no clear detections of H_2 lines in our J band spectra due to both strong atmospheric effects and some overlap of this band with higher orders in the spectrograph.

An estimation of the extinction towards HD 200775, the exciting star of NGC 7023, is complicated by the fact that HD 200775 is a Herbig Ae/Be star and thus may have unusual colors and/or circumstellar dust. Values of R_V for HD 200775 range from 3.1 (Witt & Cottrell 1980) to 6.25 (Aiello et al. 1988). For this analysis, we have adopted the $R_V = 5$ reddening law of Mathis (1990) as an intermediate value and have used $E(B - V) = 0.44$ (Witt & Cottrell 1980). All flux measurements quoted in subsequent analysis have been dereddened using this extinction law. The effects of extinction on our results is discussed in §6.

3. Rotational and Vibrational Temperatures

A clear indicator of the presence of UV-pumped fluorescence is a difference in the rotational and vibrational temperatures. The rotational (or vibrational) temperature is measured from the slope of a line passing through data with different rotational (or vibrational) upper levels but the same vibrational (or rotational) upper levels on diagrams of the $\ln(N_u/g_u) - T_u$ plane, respectively (e.g. Figures 3 and 4). Thermal excitation, with an OPR of 3, will give similar rotational and vibrational temperatures, while fluorescence is characterized by a high vibrational temperature and a low rotational temperature (e.g. Tanaka et al. 1989).

Figures 3 and 4 show that both positions observed in NGC 7023 are characterized by high vibrational temperatures (~ 5000 K) and low rotational temperatures (~ 1000 K). Our calculated rotation temperature is higher than the value derived by LeMaire et al. (1996), ~ 500 K, but is still within the uncertainties of their $1 - 0$ S(2) data. Tables 2 and 3 show the calculated vibrational and rotational temperatures between neighboring ortho and para states for several of the higher signal-to-noise transitions. This difference between rotational and vibrational temperatures was predicted by Black & Dalgarno (1976) and Black & van Dishoeck (1987) and is a definite indicator of the prescence of fluorescent emission (see Burton (1992) for a review and in particular Figure 4 of that paper).

4. Ortho-to-Para Ratio

The ortho-to-para ratio (OPR) of molecular hydrogen is the ratio of the total column density of ortho-H_2 (odd J) to para-H_2 (even J), divided by their respective statistical weights. The statistical weight of the ortho and para states, g_u, is the product of the rotational ($g_J = 2J + 1$) and spin ($g_s = 1$ for even J and 3 for odd J) degeneracies.

When H_2 is formed on the surface of grains in molecular clouds, it is usually assumed to initially have an OPR of 3 (see e.g. Spitzer & Zweibel 1974). After formation, the OPR can evolve with time, either while still on the grain surface (Tielens & Allamandola 1987), or after ejection into the gas phase, depending upon the conditions inside the cloud (Dalgarno et al. 1973; Flower & Watt 1984; Hasegawa et al. 1989; Tanaka et al. 1989; Chrysostomou et al. 1993). Exchange reactions with atomic hydrogen and H^+ can alter the OPR (Dalgarno, Black & Weisheit 1973; Flower & Watt 1984), though in regions with low H^+ number density, such as NGC 7023, reactions involving atomic hydrogen will dominate

and the rate of this reaction will strongly depend on the temperature (Takayanagi et al. 1987). For high temperatures, the OPR will be 3, while much lower values may occur for T $\lesssim 200$ K (Burton et al. 1992). Furthermore, if a photodissociation front is exposing new, cool material to the warm UV field faster than these exchange reactions can drive the OPR towards 3, a low OPR could be maintained (Chrysostomou et al. 1993). The OPR thus may reflect the formation conditions or may indicate that exchange reactions are taking place. Values in the range $1 - 1.8$ have been observed in fluorescent H_2 sources (Tanaka et al. 1989; Ramsay et al. 1993; Chrysostomou et al. 1993; Hora & Latter 1996).

In Figures 3 and 4 we show $\ln(N_u/g_u)$ vs. T_u derived from our dereddened spectra of NGC 7023. The excitation temperature of the upper level (Dabrowski 1984) is equal to the energy of the upper level divided by Boltzmann's constant ($T_u = E_u/k$), and N_u is the column density of the upper level. Based upon an examination of such a plot alone, it is possible to determine a great deal about the nature of the PDR. We plot different symbols for ortho (filled points) and para (open points) H_2 in Figures 3 and 4 to illustrate the effect of the OPR. When ortho and para measurements for a given vibrational state fall on the same line, this corresponds to an OPR of 3 and is indicative of thermal processes. If the derived level populations of ortho and para states for a given vibrational state separate vertically in the $\ln(N_u/g_u) - T_u$ plane, the OPR is different from 3, as is often observed for UV fluorescence.

Following the method outlined by Tanaka et al. (1989), we computed the vertical separation between the $J = 3$ and 4 levels by a least-squares fit through the neighboring para or ortho pair of points on the diagram, respectively, for $v = 1$. We did not use $v = 2$ due to telluric contamination in the $2 - 1$ S(2) line (Everett 1997). We obtained an OPR of 2.5 ± 0.3 for Position 1 and an OPR of 2.4 ± 0.5 for Position 2. Both of these values are intermediate between the values for thermalized gas (3) and those observed for fluorescent emission ($1 - 1.8$), where the difference from 3 is primarily driven by the $J = 2$ level. Though there is clear evidence that significant fluorescent emission is occurring in NGC 7023 (see, e.g. §3), the fact that our values for the OPR are higher than has been previously observed in fluorescent H_2 sources may indicate that additional thermal processes, such as contributions from shocks, are contributing to the chemistry of this PDR. This calculation of the OPR for NGC 7023 shows how the OPR can be a useful tool to investigate the nature of PDRs and that the interpretation of the OPR ratio can be complicated by the presence of shocks, which can mimic the behavior of warm gas.

5. Models

Based on the previous observations of NGC 7023 outlined in the introduction, the incident UV flux has a possible range of $G_0 = 10^3$ to 10^4, while the density of the surrounding material has a possible range of 10^2 cm^{-3} in the more diffuse regions to 10^5 cm^{-3} in the denser regions near HD 200775. We can also use our observed $1 - 0$ S(1) line intensity as an additional constraint in modeling the PDR in the two molecular filaments we investigate here by eliminating models which predict $1 - 0$ S(1) intensities differing by more than 3σ (or a factor of 14) from our observed intensities.

If NGC 7023 is composed of low-density, UV-illuminated clouds ($n < 10^4$ cm^{-3}), it will show fluorescent H$_2$ emission (Black & van Dishoeck 1987). In UV-illuminated clouds with densities above the critical density, $n > 10^5$ cm^{-3}, collisional deexcitation occurs faster than radiative decay and this causes some H$_2$ line ratios to approach values for thermal excitation (Sternberg & Dalgarno 1989; Burton et al. 1990; Draine & Bertoldi 1996). Draine & Bertoldi (1996) have found a density of 10^5 cm^{-3} to provide the best agreement with NGC 2023, showing that collisional deexcitation dominates over the radiative fluorescent cascade in this case. If there is a bipolar outflow in NGC 7023, this could heat the gas by shocks, giving rise to a thermal component of H$_2$ emission.

To determine the nature of the molecular filaments in NGC 7023, we have compared our dereddened flux measurements to the PDR models of Draine & Bertoldi (1996), which include both radiative transfer and the best available collisional data. The basic characteristics of all the best-fitting models described in the text are summarized in Table 4. Draine & Bertoldi (1996) present models ranging from $n = 10^2$ to 10^6 cm^{-3} and in UV flux from $G_0 = 1$ to 10^5. In addition to single model fits, we have also mixed the models of Draine & Bertoldi (1996) with the thermal models of Black & van Dishoeck (1987). These thermal models, referred to as S1 and S2, represent shock-excited gas at temperatures of 1000 and 2000 K, respectively.

In order to compare our data with these models, we computed the value of $\ln(N_u/g_u)$ normalized to the $1 - 0$ S(1) line for each model and our data. We then calculated χ^2 to determine the goodness of fit. Our χ^2 parameter was calculated by varying only one free parameter, the overall intensity. The uncertainty used in calculating χ^2 only reflects uncertainties in the relative line intensities. We considered any model with $\chi^2 \leq \chi^2_{min} + 1$, where χ^2_{min} corresponds to the best-fitting model for that filament, to be a reasonable fit (Bevington & Robinson 1992). We note that our χ^2 value indicates which models give the best overall agreement with our observations, but does not indicate which regions of the $\ln(N_u/g_u) - T_u$ plane were in good or poor agreement. The 10 lines used in our analysis were $v = 1$, $J = 2 - 5$; $v = 2$, $J = 2, 3$, and 5; and $v = 3$, $J = 3 - 5$. As mentioned above, the $2 - 1$ S(2) line was excluded as it lies near a contaminating telluric feature (Everett

1997). In addition, although the $3 - 2$ S(2) line intensity was not above the 3σ detection limit at Position 2, we used the measured flux and associated error to include this line in the χ^2 calculation. The results of these calculations are listed in Table 4 along with the physical characteristics of the best-fitting models.

We next considered mixtures of models. To mix two models together, we normalized the flux predictions for each separate model to the $1 - 0$ S(1) line and multiplied each model by its percentage contribution to the final mixture. This mixture was then converted to $\ln(N_u/g_u)$ format and χ^2 was calculated as described above. When mixing two models, we stepped from 0% to 99% contribution of the second model in 1% increments. We explored fluorescent models, at a range of densities, mixed with thermal models. We also examined low-density fluorescent models mixed with high-density fluorescent models. Table 5 lists our results for mixtures of fluorescent/collisional models with a thermal component. In our analysis, we excluded all models with a $1 - 0$ S(1) intensity less than $\sim 2 \times 10^{-5}$ erg s^{-1} cm^{-2} sr^{-1} based on our flux calibration. Table 6 lists our results for mixtures of the models of Draine & Bertoldi (1996) with their high-density ($n = 10^6$ cm^{-3}) model (Qm3o). Mixtures of this model with lower-density models produced the best fits to our data of all of our high + low-density combinations.

6.   Discussion

For Position 1, the model comparisons presented in Tables 4, 5, and 6 show that a mixture of a warm component with fluorescent emission fits somewhat, but not significantly, better than pure fluorescent emission. The improvement in the fit is $\Delta\chi^2 = 1.4$, where $\Delta\chi^2 = 1$ corresponds to 1σ (Bevington & Robinson 1992). The warm component which improves the fit is equally well characterized by a high density fluorescent model, with $n = 10^6$ cm^{-3} and $G_0 = 10^4$, or by a thermal model with $T = 1000 - 2000$ K. The best-fitting mixed models have $n = 10^4 - 10^5$ cm^{-3} and $G_0 = 1000 - 5000$ for the low-density fluorescent component. The best-fit pure fluorescent models, not surprisingly, have values that are intermediate between the values for the low-density and high-density components of the best-fit mixed models: $n = 10^5 - 10^6$ cm^{-3} and $G_0 = 10^3 - 10^4$.

For Position 2, the data were equally well fit by pure fluorescent models or by mixtures of a warm component with fluorescent emission ($\Delta\chi^2 \leq 1$). In all cases, the best-fit models have $n = 10^4 - 10^5$ cm^{-3} and $G_0 = 10^3$.

The best-fit models as determined by the χ^2 results in Tables 4 through 6 are slightly dependent upon the extinction. As the rotational and vibrational quantum numbers, v and

J, decrease with increasing wavelength (see e.g. Table 1), a larger value of the extinction increases the intensity of the lower (shorter wavelength) transitions over the upper (longer wavelength) transitions. Thus an underestimation of the extinction can mimic the effect of adding a higher-temperature thermal component or a higher-density collisional component to the excitation. We found, however, that assuming either no extinction or twice our adopted value ($2 \times E(B - V) = 0.88$) changes our results in Tables 4, 5, & 6 by $\Delta\chi^2 < 1$ (less than 1σ).

As mentioned in the previous section, our χ^2 parameter only tells us approximately which models provide the best agreement to the data and no information on the behavior of individual components of the spectrum. In addition, the χ^2 parameter only includes the uncertainties in our relative line intensity measurements, and does not reflect possible uncertainties in the models or the effects of a more complex geometry than were employed in the model calculations. One way of extracting information about areas of specific disagreement is to test the data and models for lines ratios most strongly affected by a warm component.

Figure 5 shows a plot of the $2 - 1$ S(1)/$1 - 0$ S(1) vs. $2 - 1$ S(3)/$1 - 0$ S(3) line ratios and includes both our data and representative models from Table 4. Figure 5 also shows the behavior of these line ratios for the $n = 10^4$ cm^{-3}, $G_0 = 10^3$ model (Hw3o) of Draine & Bertoldi (1996) as it is mixed with greater percentages of two thermal models (Black & van Dishoeck 1987). These lines are well-suited to testing the contribution of a thermal component to a fluorescent model as the addition of a thermal component to a fluorescent model tends to enhance the $v = 1$ odd J levels in the spectrum as it pushes the OPR towards 3, but has less effect on the $v = 2$ odd J levels, as the thermal component contributes most to the lower-lying levels. The rotational temperatures for the $v = 1$ levels (except for $J = 4 - 2$) are also higher than those of the $v = 2$ and 3 levels, providing further evidence of the presence of a second, possibly thermal, component. This figure provides some tantalizing evidence that there is a thermal component to the emission that further investigation with higher signal-to-noise data or a greater number of lines could resolve.

Figure 5 also shows that none of the pure fluorescent models, and none of the mixtures of fluorescence with a thermal component or a higher-density component, can explain the very strong $1 - 0$ S(3) emission we observe. It is possible that this line is blended with some other unknown line, or that we have underestimated the uncertainties in the atmospheric correction at this wavelength. As a check, we compared all the models in Tables 4, 5, and 6 to our observations with the $1 - 0$ S(3) line excluded. The minimum χ^2 values improve significantly ($\chi^2_{min} = 1.3$ for Position 1 and 2.9 for Position 2), but our overall conclusions concerning the density and excitation in NGC 7023 are unchanged.

7. Conclusion

Analysis of the near-infrared lines of molecular hydrogen in NGC 7023 has shown that the best-fit pure fluorescent models for Position 1 have $n = 10^5 - 10^6$ cm^{-3} and $G_0 = 10^3 - 10^4$. The model fits are somewhat improved (1.4σ) by a mixture of models involving a fluorescent model with $n = 10^4 - 10^5$ cm^{-3} and $G_0 = 1000 - 5000$ and a warm component. This warm component could be either a higher-density, fluorescent model $(n = 10^6$ cm^{-3}, $G_0 = 10^4)$, perhaps due to dense clumps in the PDR, or a model reflecting a thermal contribution, possibly due to shocks. In Position 2, the best-fitting models have $n = 10^4$ cm^{-3} and $G_0 = 10^3$, with our data equally well fit by fluorescence with or without a warm component. Our derived densities, $n = 10^4 - 10^5$ cm^{-3} Position 1 and 10^4 cm^{-3} in Position 2, are in good agreement with previously determined densities of $4 \times 10^3 - 10^5$ cm^{-3}. The suggestion of a warm component in Position 1 may either point to high-density clumps (10^6 cm^{-3}) or suggest shocks due to a bipolar outflow.

REFERENCES

Aiello, S., Barsella, B., Chlewicki, G., Greenberg, J.M., Patriarchi, P., & Perinotto, M. 1988, A&AS, 73, 195

Bevington, P.R. & Robinson, D.K. 1992, Data Reduction and Error Analysis for the Physical Sciences (New York: McGraw Hill), p. 145

Black, J.H. & Dalgarno, A. 1976, ApJ, 203, 132

Black, J.H., Porter, A., & Dalgarno, A. 1981 ApJ, 249, 138

Black, J.H. & van Dishoeck, E.F. 1987, ApJ, 322, 412

Brand, P.W.J.L., Moorhouse, A., Burton, M.G., Geballe, T.R., Bird, M., & Wade, R. 1988, ApJ, 334, L103

Brand, P.W.J.L., Toner, M.P., Geballe, T.R., Webster, A.S., Williams, P.M., & Burton, M.G. 1989, MNRAS, 236, 929

Burton, M.G., Hollenbach, D.J., & Tielens, A.G.G.M. 1990, ApJ, 365, 620

Burton, M.G. 1992, Aust.J.Phys., 45, 463

Burton, M.G., Hollenbach, D.J., & Tielens, A.G.G.M. 1992, ApJ, 399, 563

Cesarsky, D., Lequeux, J., Abergel, A., Perault, M., Palazzi, E., Madden, S., & Tran, D. 1996, A&A, 315, L309

Chokshi, A., Tielens, A.G.G.M., Werner, M.W., & Castelaz, M.W. 1988, ApJ, 334, 803

Chrysostomou, A., Brand, P.W.J.L., Burton, M.G., & Moorhouse, A. 1993, MNRAS, 265, 329

Dabrowski, I. 1984, Can. J. Phys., 62, 1639

Dalgarno, A., Black, J.H., & Weisheit, J.C. 1973, *Ap. Letters*, 14, 77

Draine, B.T. & Bertoldi, F. 1996, ApJ, 468, 269

Elias, J.H., Frogel, J.A., Matthews, K., & Neugebauer, G. 1982, AJ, 87, 1029

Everett, M. 1997, in press

Flower, D.R. & Watt, G.D. 1984, MNRAS, 209, 25

Fuente, A., Martin-Pintado, J., Cernicharo, J., & Bachiller, R. 1993, A&A, 276, 473

Fuente, A., Martin-Pintado, R., Neri, R., Rogers, C., & Moriarty-Schieven, G. 1996, A&A, 310, 286

Gatley, I., Hasegawa, T., Suzuki, H., Garden, R., Brand, P., Lightfoot, J., Glencross, W., Okuda, H., & Nagata, T. 1987, ApJ, 318, L73

Gautier, T.N., Fink, U., Treffers, R.R., & Larson, H.P. 1976, ApJ, 207, L129

Goldschmidt, O. & Sternberg, A. 1995, ApJ, 439, 256

Habing, H.J. 1968, Bull. Astr. Inst. Netherlands, 19, 421

Hasegawa, T., Gatley, I., Garden, R.P., Brand, P.W.J.L., Ohishi, M., Hayashi, M., & Kaifu, N. 1989, ApJ, 318, L77

Hodapp, K., Hora, J.L., Irwin, E., & Young, T. 1995, PASP, 106, 87

Hollenbach, D. & McKee, C.F. 1979, ApJS, 41 555

Hollenbach, D. & McKee, C.F. 1989, ApJ, 342, 306

Hollenbach, D.J., Takahashi, T., & Tielens, A.G.G.M. 1991, ApJ, 377, 192

Hora, J.L. & Latter, W.B. 1996, ApJ, 461, 288

LeMaire, J.L., Field, D., Gerin, M., Leach, S., Pineau des Forêts, G., Rostas, F., & Rouan, D. 1996, A&A, 308, 895

Mathis, J.S. 1990, ARA&A, 28, 37

Ramsay, S.K., Chrysostomou, A., Geballe, T.R. Brand, P.W.J.L., & Mountain, M. 1993, MNRAS, 263, 695

Rogers, C., Heyer, M.H., & Dewdney, P.E. 1995, ApJ, 442, 694

Sellgren, K. 1983, AJ, 88, 985

Sellgren, K. 1986, ApJ, 305, 399

Spitzer, L., & Zweibel, E.G. 1974, ApJ, 191, L127

Sternberg, A. & Dalgarno, A. 1989 ApJ, 338, 197

Stover, R.J. 1988, in Instrumentation for Ground-Based Optical Astronomy: Present and Future, ed. L.B. Robinson, (New York: Springer-Verlag), 443

Takayanagi, K., Sakimoto, K., & Onda, K. 1987, ApJ, 318, L81

Tanaka, M., Hasegawa, T., Hayashi, S.S., Brand, P.W.J.L., & Gatley, I. 1989, ApJ, 336, 207

Tielens, A.G.G.M. & Hollenbach, D.J. 1985, ApJ, 291, 722

Tielens, A.G.G.M. & Allamandola, L.J. 1987, in Interstellar Processes, ed. D.J. Hollenbach & H.A. Thronson (Reidel: Dordrecht), p. 397

Treffers, R.R., Fink, U., Larson, H.P., & Gautier, T.N. 1976, ApJ, 209, 793

Turner, J., Kirby-Docken, K., & Dalgarno, A. 1977, ApJS, 35, 281

Watkin, S., Gledhill, T.M., & Scarrott, S.M. 1991, MNRAS, 252, 229

Watt, G.D. 1983, MNRAS, 205, 321

Watt, G.D., Burton, W.B., Choe, S.-U., & Liszt, H.S. 1986, A&A, 163, 194

Witt, A.N. & Cottrell, M.J. 1980, ApJ, 235, 899

TABLE 1

Normalized Line Intensities

Transition	Wavelength(μm)	Position 1		Position 2	
		Intensity	σ_I	Intensity	σ_I
$1 - 0$ S(7)	1.7475	0.199	$\pm$ 0.040	0.250	$\pm$ 0.050
$1 - 0$ S(6)[1]	1.7876	<0.21		<0.18	
$2 - 1$ S(5)	1.9443	0.299	$\pm$ 0.037	0.225	$\pm$ 0.029
$1 - 0$ S(3)	1.9570	1.237	$\pm$ 0.085	1.103	$\pm$ 0.086
$2 - 1$ S(4)[1]	2.0035	<0.10		0.093	$\pm$ 0.030
$7 - 5$ O(5)	2.0215	0.063	$\pm$ 0.020	0.125	$\pm$ 0.030
$1 - 0$ S(2)	2.0332	0.377	$\pm$ 0.025	0.400	$\pm$ 0.038
$8 - 6$ O(3)	2.0412	0.071	$\pm$ 0.020	<0.09	
$3 - 2$ S(5)	2.0650	0.111	$\pm$ 0.025	<0.110	
$2 - 1$ S(3)	2.0729	0.293	$\pm$ 0.021	0.249	$\pm$ 0.030
$1 - 0$ S(1)	2.1213	1.000	$\pm$ 0.039	1.000	$\pm$ 0.043
$3 - 2$ S(4)	2.1274	<0.09		<0.09	
$2 - 1$ S(2)[1]	2.1536	0.161	$\pm$ 0.020	0.148	$\pm$ 0.025
$3 - 2$ S(3)	2.2008	0.147	$\pm$ 0.018	0.109	$\pm$ 0.030
$1 - 0$ S(0)	2.2227	0.383	$\pm$ 0.025	0.463	$\pm$ 0.049
$2 - 1$ S(1)	2.2471	0.325	$\pm$ 0.028	0.446	$\pm$ 0.028
$3 - 2$ S(2)	2.2864	0.081	$\pm$ 0.017	0.060[2]	$\pm$ 0.030
$2 - 1$ S(0)	2.3550	0.186	$\pm$ 0.018	0.286	$\pm$ 0.026
$3 - 2$ S(1)	2.3858	0.245	$\pm$ 0.025	0.268	$\pm$ 0.028
$1 - 0$ Q(1)	2.4059	1.800	$\pm$ 0.086	1.651	$\pm$ 0.074
$1 - 0$ Q(2)	2.4128	0.661	$\pm$ 0.051	0.708	$\pm$ 0.041

[1] This line may suffer contamination by telluric absorption.

[2] Non-detection: measured line intensity is less than the 3σ limit.

Table 1: Normalized line intensities for Positions 1 and 2 in NGC 7023. Position 1 is 40″ W, 34″ N of HD 200775 and Position 2 is 22″ W, 66″ S of HD 200775. Columns 1 and 2 list the molecular transitions and vacuum wavelengths (after Black & van Dishoeck 1987) for the emission lines. Columns 3 and 4 list the intensities and 1σ errors for lines at Position 1. The intensities have been normalized with respect to the $1 - 0$ S(1) intensity of $5.43 \pm 1.64 \times 10^{-4}$ ergs cm^{-2} s^{-1} sr^{-1}. Columns 5 and 6 list the intensities and 1σ errors for emission lines at Position 2. These intensities have been normalized with respect to the

$1 - 0$ S(1) intensity of $2.58 \pm 0.78 \times 10^{-4}$ ergs cm^{-2} s^{-1} sr^{-1}. The uncertainties in the $1 - 0$ S(1) intensity include loss at the slit but do not reflect the uncertainty in the overall flux calibration (see §2). All upper limits are 3σ limits.

TABLE 2

Rotation Temperature

Transition	Level 1	Level 2	Position 1		Position 2	
			T_{rot}	σ_T	T_{rot}	σ_T
$J = 4 - 2$	$1 - 0$ S(0)	$1 - 0$ S(2)	970	$\pm$ 80	870	$\pm$ 130
$J = 5 - 3$	$1 - 0$ S(1)	$1 - 0$ S(3)	2750	$\pm$ 450	2240	$\pm$ 500
$J = 9 - 5$	$1 - 0$ S(3)	$1 - 0$ S(7)	2080	$\pm$ 210	2480	$\pm$ 330
$J = 5 - 3$	$2 - 1$ S(1)	$2 - 1$ S(3)	1710	$\pm$ 330	1060	$\pm$ 120
$J = 5 - 3$	$3 - 2$ S(1)	$3 - 2$ S(3)	1120	$\pm$ 160	830	$\pm$ 160

Table 2: Rotation temperatures for H_2 emission in NGC 7023 calculated from the relative line strengths for the listed transitions with associated 1σ uncertainties.

TABLE 3

Vibration Temperature

Transition	Level 1	Level 2	Position 1		Position 2	
			T_{vib}	σ_T	T_{vib}	σ_T
$v = 2-1$	$2-1$ S(0)	$1-0$ S(0)	5410	$\pm$ 610	7040	$\pm$ 1660
$v = 2-1$	$2-1$ S(1)	$1-0$ S(1)	3920	$\pm$ 260	5030	$\pm$ 430
$v = 2-1$	$2-1$ S(3)	$1-0$ S(3)	3250	$\pm$ 280	3160	$\pm$ 320
$v = 3-2$	$3-2$ S(3)	$2-1$ S(3)	8580	$\pm$ 2490	7010	$\pm$ 2840

Table 3: Vibration temperatures for H_2 emission in NGC 7023 calculated from the relative line strengths for the listed transitions with associated 1σ uncertainties.

TABLE 4

Model Characteristics

Model	χ^2		n_H	G_0	T_{gas}	$I_{1-0S(1)}$
	Position 1	Position 2	cm^{-3}	(Habings)	(K)	erg s^{-1} cm^{-2} sr^{-1}
Hw3o	12.	**4.4**	10^4	10^3	500	1.85×10^{-5}
Hh3o	8.0	**5.1**	10^4	10^3	1000	2.20×10^{-5}
Lm3o	7.5	**5.2**	10^5	10^3	300	2.61×10^{-5}
Lw3o	**6.2**	5.5	10^5	10^3	500	2.69×10^{-5}
Mw3o	8.1	8.3	10^5	10^4	500	9.66×10^{-5}
Mh3o	**6.7**	9.4	10^5	10^4	1000	1.17×10^{-4}
Qm3o	**6.4**	11.	10^6	10^4	300	1.32×10^{-4}
Qw3o	9.2	12.	10^6	10^4	500	1.42×10^{-4}
n2023a	7.3	7.9	10^5	5000	500	3.29×10^{-4}

Table 4: Basic characteristics of the best-fitting models of Draine & Bertoldi (1996) compared to Positions 1 and 2 in NGC 7023. The χ^2 values listed are reduced χ^2. All χ^2 calculations were performed with the column densities derived from the dereddened intensities for the 10 H$_2$ lines listed in the text. Values of χ^2 in bold type are those with $\chi^2 \leq \chi^2_{min} + 1$, where χ^2_{min} is the minimum value of χ^2 for each position. The density, n_H, is the nucleon density, G_0 is the UV flux in the units of the interstellar radiation field (Habing 1968), T_{gas} is the gas temperature, and $I_{1-0S(1)}$ is the intensity of the $1 - 0$ S(1) line.

TABLE 5

Best Fit Results for Mixes with a Thermal Component

Models	Position 1 + S1		Position 1 + S2		Position 2 + S1		Position 2 + S2	
	χ^2	% S1	χ^2	% S2	χ^2	% S1	χ^2	% S2
Hw3o	8.7	28	**5.2**	35	**3.9**	16	**3.6**	18
Hh3o	6.8	18	**5.4**	25	5.1	6	5.1	6
Lm3o	6.3	18	**4.9**	25	5.1	6	5.1	6
Lw3o	**5.6**	13	**4.8**	20	5.5	2	5.5	0
Mw3o	7.0	18	6.4	22	8.2	7	8.3	4
Mh3o	6.7	0	6.7	0	9.4	0	9.4	0
Qm3o	6.4	0	6.4	0	11.	0	11.	0
Qw3o	9.2	0	9.2	0	12.	0	12.	0
n2023a	6.4	16	6.0	19	7.8	5	7.9	1

Table 5: The best-fit results from a comparison of our observations of Positions 1 and 2 in NGC 7023 to mixtures of fluorescent models of stationary PDRs (Draine & Bertoldi 1996) and thermal models (Black & van Dishoeck 1987). S1 and S2 correspond to shock-heated gas at 1000 K and 2000 K, respectively. Column 1 lists the models described in detail in Table 4. Columns 2 and 3 list the χ^2 values and % of model S1 in the best-fitting mixture of these two models to Position 1. Columns 4 and 5 list the same for mixtures of the models in Column 1 and model S2. The last four columns repeat columns 2 through 5 but for Position 2. Values of χ^2 in bold type are those with $\chi^2 \leq \chi^2_{min} + 1$, where χ^2_{min} is the minimum value of χ^2 for each position.

TABLE 6

Mixes of a Low + High Density Component

Models	Position 1 + Qm3o		Position 2 + Qm3o	
	χ^2	% Qm3o	χ^2	% Qm3o
Hw3o	**4.8**	71	**4.3**	12
Hh3o	**5.0**	62	**5.1**	0
Lm3o	**5.1**	60	**5.2**	0
Lw3o	**5.0**	51	5.5	0
Mw3o	5.9	71	8.3	0
Mh3o	6.1	58	9.4	0
Qw3o	9.2	0	11.	65
n2023a	**5.8**	63	7.9	0

Table 6: The best-fit results from a comparison of observations of Positions 1 and 2 in NGC 7023 to mixtures of models from Draine & Bertoldi (1996) with their $n = 10^6$ cm^{-3}, $G_0 = 10^4$ model (Qm3o). Column 1 lists the models described in detail in Table 4. Columns 2 and 3 list the χ^2 values and % of model Qm3o in the best-fitting mixture of these models to Position 1. Columns 4 and 5 list the same for Position 2. Values of χ^2 in bold type are those with $\chi^2 \leq \chi^2_{min} + 1$, where χ^2_{min} is the minimum value of χ^2 for each position.
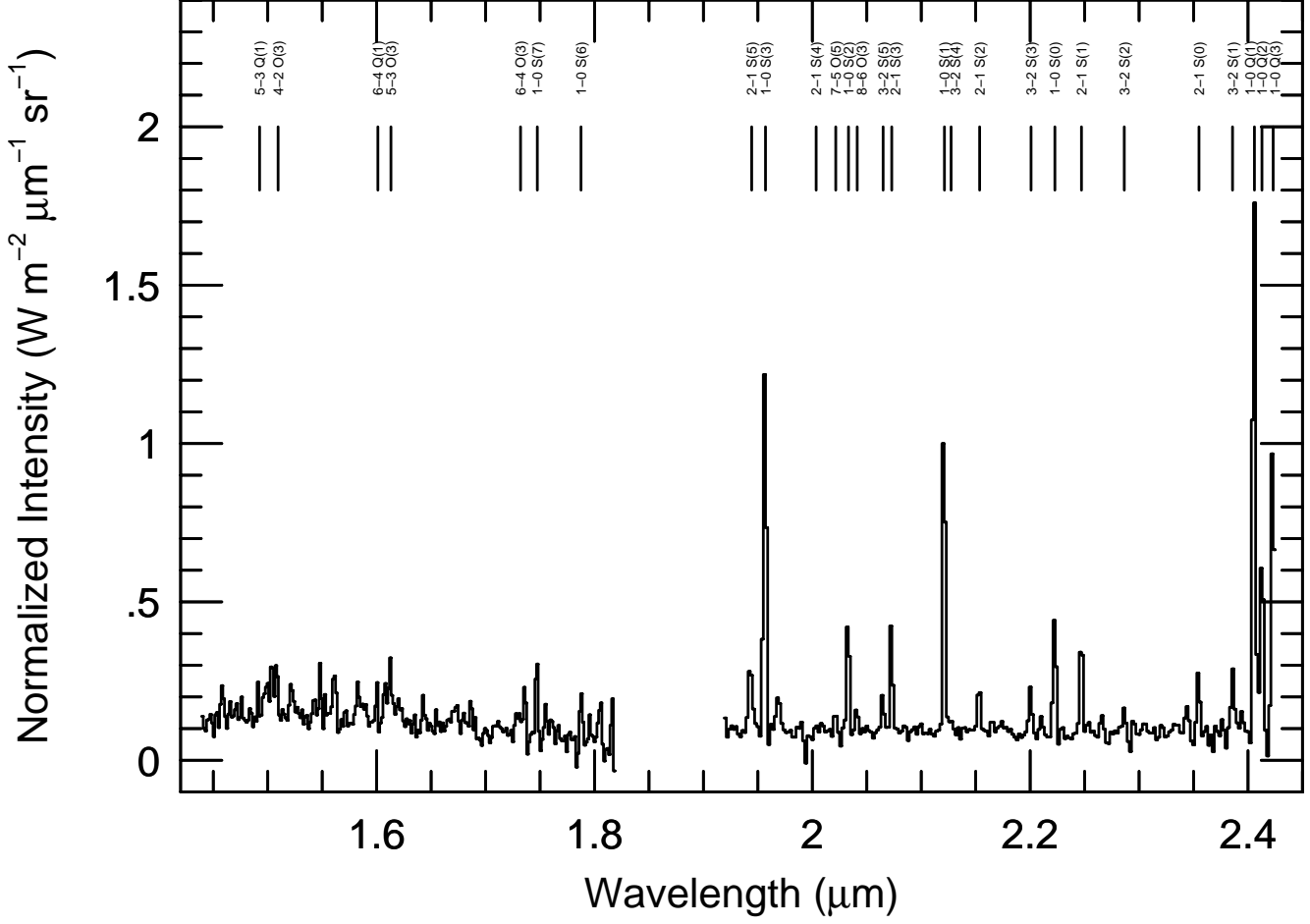
Fig. 1.— H and K band spectra of Position 1 in NGC 7023. Position 1 is located $40''$ West, $34''$ North of the central star, HD 200775. The wavelengths of molecular hydrogen lines have been labeled above the spectrum. The spectral resolution is $\lambda/\Delta\lambda = 730$ in K and 720 in H. The intensity has been normalized to the peak $1 - 0$ S(1) intensity.
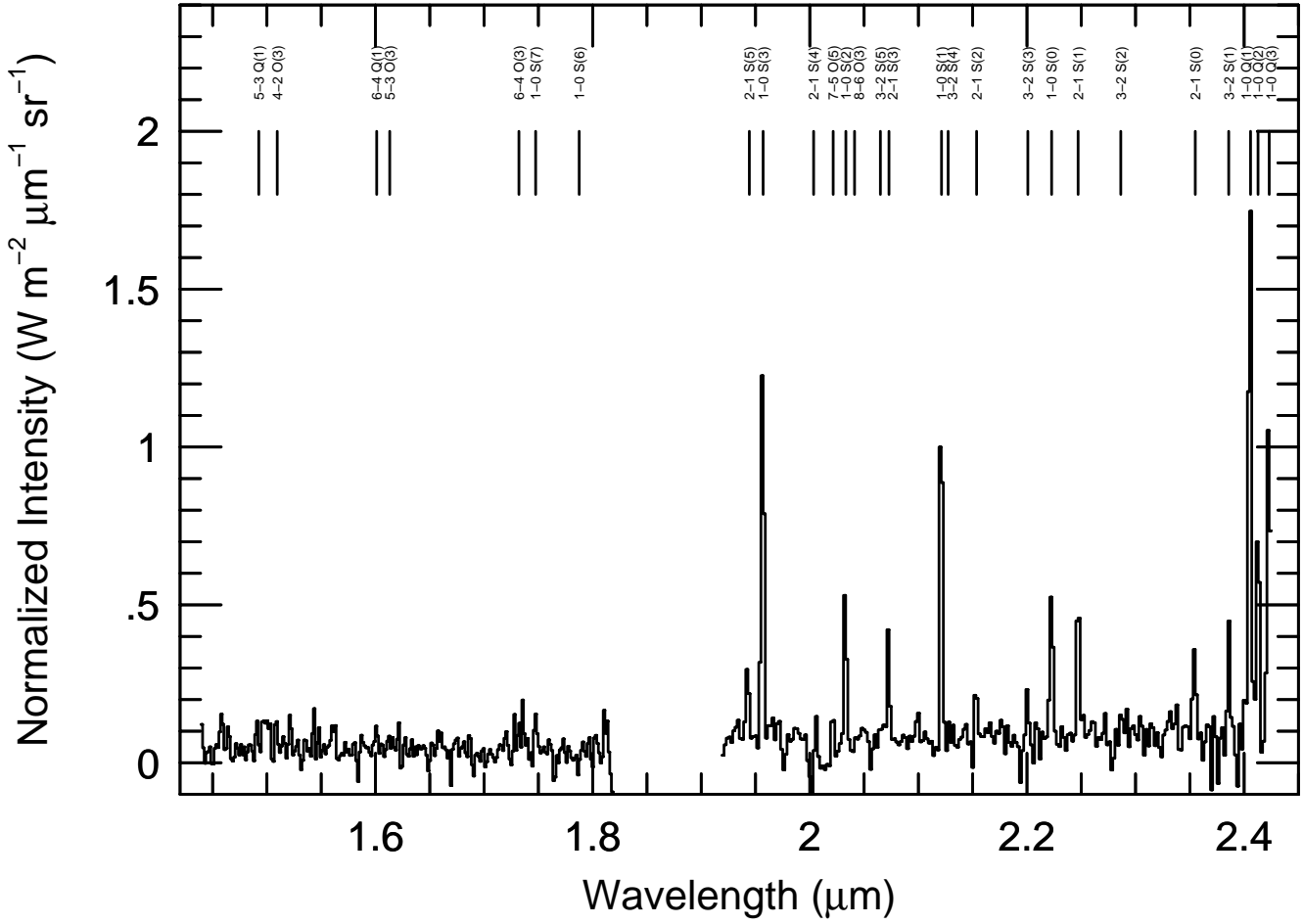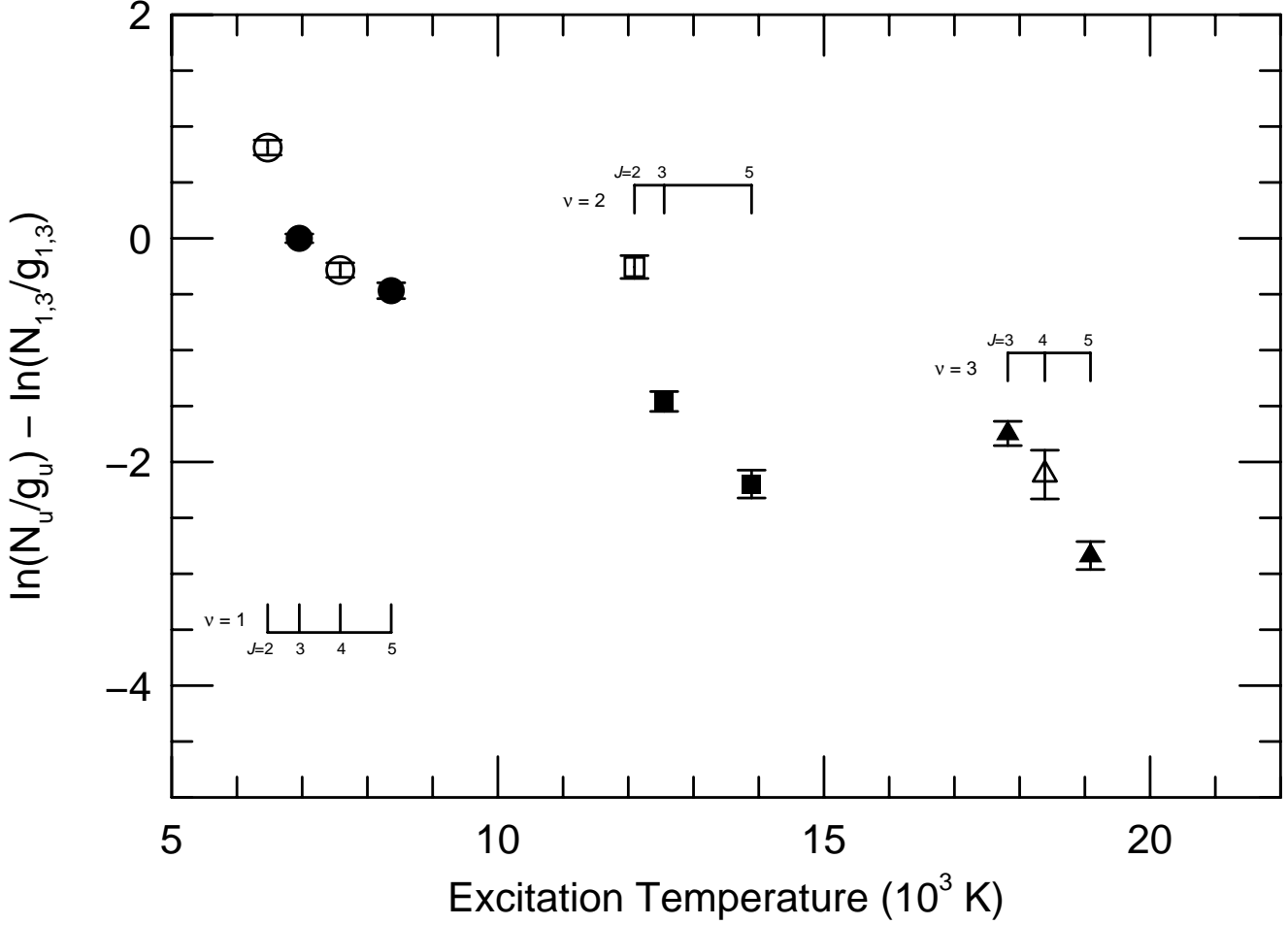
Fig. 2.— H and K band spectra of Position 2 in NGC 7023. Position 2 is located 22″ West, 66″ South of the central star, HD 200775. The wavelengths of molecular hydrogen lines have been labeled above the spectrum as in Figure 1. The spectral resolution is $\lambda/\Delta\lambda = 730$ in K and 720 in H. The intensity has been normalized to the peak $1 - 0$ S(1) intensity.

Fig. 3.— Diagram of $\ln(N_u/g_u)$ vs. T_u for Position 1 in NGC 7023 for the 10 lines used in our analysis and based upon the data recorded in Table 1 after dereddening. The y−axis shows the log of the column density of molecular hydrogen in a given state, N_u, divided by the statistical weight, g_u, and normalized to the $1 - 0$ S(1) transition ($v = 1, J = 3$). The x−axis gives the excitation temperature, T_u, of the upper level of a given transition after Dabrowski (1984). Circles denote transitions from the $v = 1$ vibrational state, squares from $v = 2$, and triangles from $v = 3$. Open symbols represent para (even J) rotational transitions, filled symbols represent ortho (odd J) transitions. All errorbars are 1σ errors. Upper limits shown are 3σ upper limits.
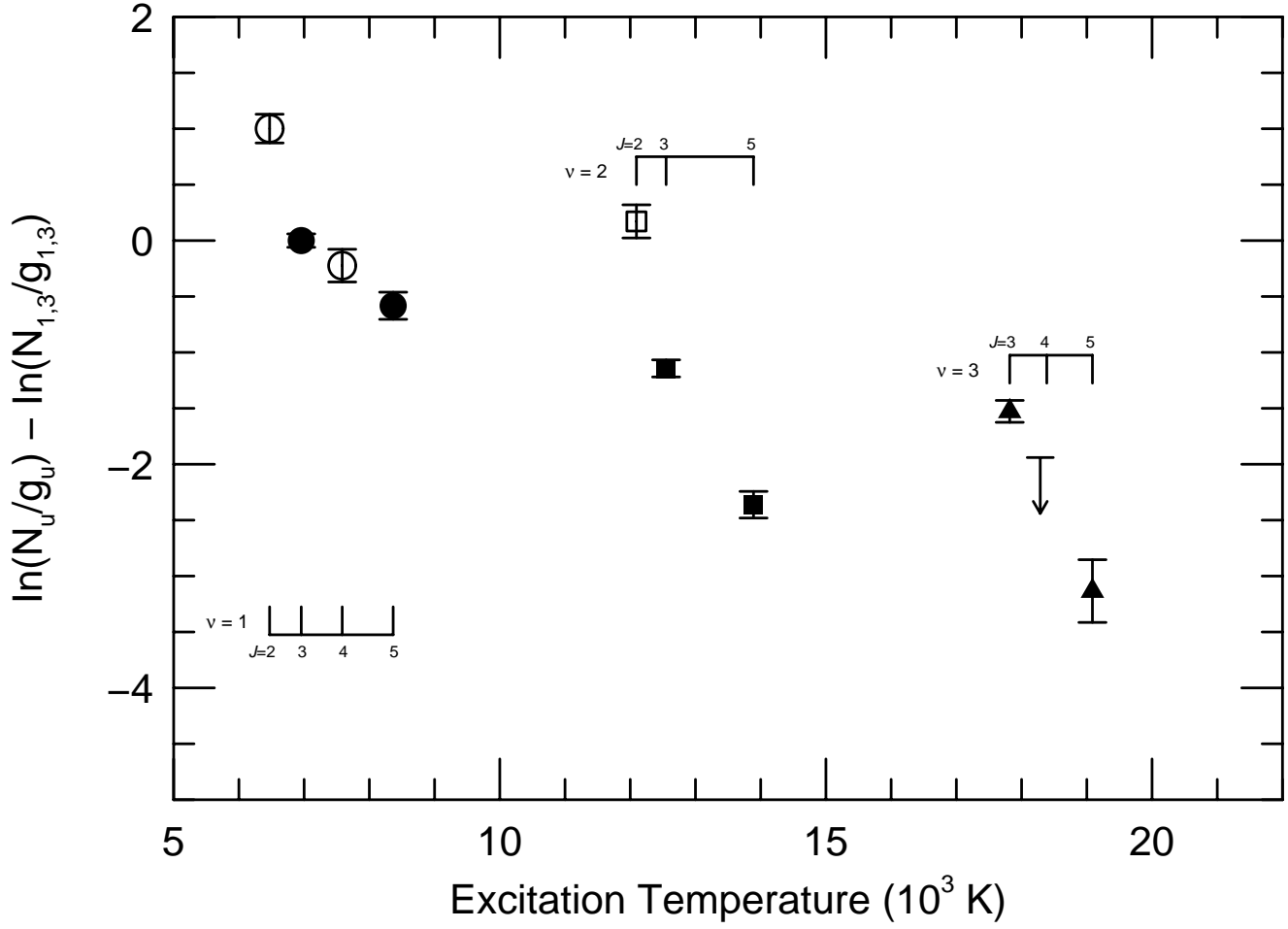
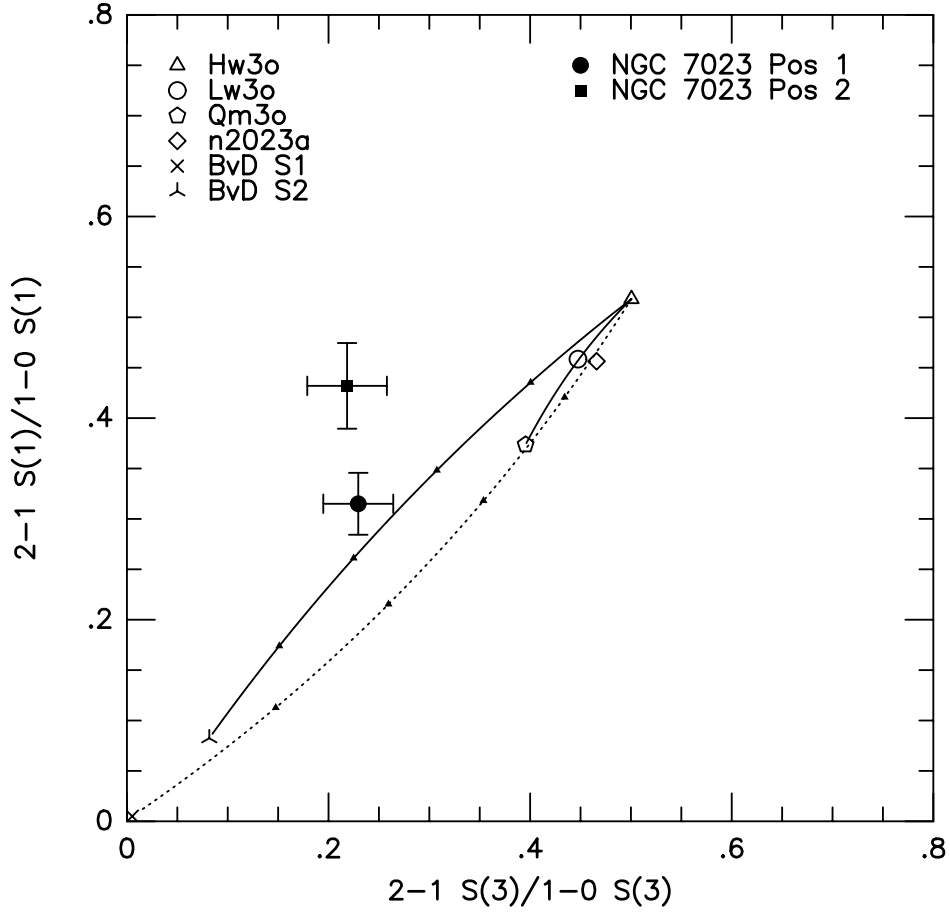Fig. 4.— Same as Figure 3, except for line strengths measured in Position 2 of NGC 7023.

Fig. 5.— Ratio of the $2-1$ S(1)/$1-0$ S(1) lines vs. ratio of the $2-1$ S(3)/$1-0$ S(3) lines of H_2 for our observations of Position 1 and 2 in NGC 7023 (with 1σ errorbars) and a selection of the models listed in Table 4. All models from Table 4 not shown have similar line ratios to the illustrated model at the same density but different UV illumination and gas temperature. These ratios represent low, odd rotational transitions where the effects of a thermalized component would be most readily noticed (see §6). Also shown are the way the line ratios change for model Hw3o of Draine & Bertoldi (1996) with the addition of the 1000 and 2000 K thermal models of Black & van Dishoeck (1987), and wth the high-density model Qm3o (see §6). Tick marks denote 20, 40, 60, and 80% contributions of the thermal models.